Sn-mediated Ge/Ge(001) growth by low-temperature molecular-beam epitaxy: Surface smoothening and enhanced epitaxial thickness

K. A. Bratland,[a] Y. L. Foo,[b] T. Spila, H.-S. Seo, R. T. Haasch, P. Desjardins,[c] and J. E. Greene

Frederick Seitz Materials Research Laboratory and the Materials Science Department, University of Illinois, 104 South Goodwin Avenue, Urbana, Illinois 61801

(Received 5 April 2004; accepted 17 November 2004; published online 21 January 2005)

Fully strained single-crystal metastable $Ge_{1-x}Sn_x$ layers were grown on Ge(001) in order to probe the role of Sn dopant and alloy concentrations ($C_{Sn}=1\times10^{18}$ cm^{-3} to 6.1 at. %) on surface roughening pathways leading to epitaxial breakdown during low-temperature (155 °C) molecular-beam epitaxy of compressively strained films. The addition of Sn was found to mediate Ge(001) surface morphological evolution through two competing pathways. At very low Sn concentrations ($x\lesssim0.02$), the dominant effect is a Sn-induced enhancement in both the Ge surface diffusivity and the probability of interlayer mass transport. This, in turn, results in more efficient filling of interisland trenches, and thus delays epitaxial breakdown. In fact, breakdown is not observed at all for Sn concentrations in the doping regime, $1\times10^{18}\leqslant C_{Sn}<4.4\times10^{20}$ cm^{-3} ($2.3\times10^{-5}\leqslant x<0.010$)! At higher concentrations, there is a change in $Ge_{1-x}Sn_x(001)$ growth kinetics due to a rapid increase in the amount of compressive strain. This leads to a gradual reduction in the film thickness $h_1(x)$ corresponding to the onset of breakdown as strain-induced roughening overcomes the surface smoothening effects, and results in an increase in the overall roughening rate. We show that by varying the Sn concentration through the dopant to dilute alloy concentration range during low-temperature Ge(001) growth, we can controllably manipulate the surface roughening pathway, and hence the epitaxial thickness, over a very wide range. © *2005 American Institute of Physics*. [DOI: 10.1063/1.1848188]

I. INTRODUCTION

The development of a detailed atomic-level understanding of the kinetic pathways by which dopant and alloying species mediate surface morphological evolution during epitaxial growth is of interest for both scientific and technological reasons. Thin-film applications require ever better control of microstructure and surface morphology, while demanding lower growth temperatures. Unfortunately, lower growth temperatures typically result in increased defect concentrations and more rapid surface roughening rates. However, it has been well documented that the addition of selected impurities, termed surfactants, during semiconductor epitaxy can decrease surface roughness. For example, predepositing submonolayer coverages of As or Sb during Ge growth on Si(001) by molecular-beam epitaxy (MBE) has been used to inhibit Ge islanding and reduce interdiffusion at the film/substrate interface.[1–4] Similarly, dosing the surface with $\leqslant1$ monolayer of Ga prior to Si/Si(111)[5–9] growth by low-temperature MBE (LT-MBE) has been shown to reduce kinetic roughening. Despite numerous investigations of surfactant-mediated growth, however, a complete understanding of the atomic mechanisms by which a foreign adsorbate modifies the growth mode has not yet emerged.

Here, we focus on the role of dopants and alloying elements in mediating the surface reaction pathway leading to epitaxial breakdown during LT growth. We use Sn in Ge/Ge(001) as a model system to determine the effect of dilute surfactant concentrations on surface roughening and, hence, the critical film thickness h_1 corresponding to the onset of epitaxial breakdown. From a technological standpoint, $Ge_{1-x}Sn_x$ and related alloys are themselves of interest due to the potential they offer for developing totally group-IV-based optoelectronic materials systems. $Ge_{1-x}Sn_x$ has been predicted to exhibit a direct band gap in unstrained alloys, tunable from $\simeq0.55$ to 0 eV with x ranging from 0.20 to 0.65.[10,11] The crossover from an indirect to direct band-gap semiconductor with increasing Sn concentration has been experimentally verified by He *et al.*[12] and Ragan *et al.*[13]

Sn, which has previously been reported to both increase[14] and decrease[15,16] the epitaxial thickness of Ge(001), has a strong tendency to segregate to the surface during the growth of $Ge_{1-x}Sn_x(001)$ and thus requires LT deposition in a highly kinetically limited regime. The propensity for surface segregation in the $Ge_{1-x}Sn_x(001)$ system derives from both the larger covalent radius of Sn and its lower sublimation enthalpy.[17,18] While the incorporation of Sn in Ge creates compressive strain, strain-induced roughening does not typically occur during LT epitaxy due to the necessity for significant mass transport. However, Desjardins *et al.*[16] demonstrated that the thermal activation required for strain-induced roughening can be partially overcome by the fact that kinetic roughening during LT growth provides sur-

[a]IBM T. J. Watson Research Center, 1101 Kitchawan Road, Route 134, Yorktown Heights, NY 10598; electronic mail: bratland@us.ibm.com
[b]Institute of Materials Research and Engineering (IMRE), 3 Research Link, S(117602), Singapore.
[c]Départment de génie physique, École Polytechnique de Montréal, C.P. 6079, Succ. Centre-Ville, Montréal, Québec H3C 3A7 Canada.

face oscillations over lateral length scales, which are sufficient to initiate strain-induced islanding even at temperatures where it would not otherwise proceed.

Kinetic surface roughening[19–28] occurs spontaneously during LT epitaxial growth due to the combination of low adatom mobilities and the presence of Ehrlich barriers,[29] and/or deep traps, at descending step edges. The latter results in a divergence in adatom currents, giving rise to increased island nucleation on upper terraces, leading to nonlinear growth through the formation of a regular array of mounds. Both the surface width w and the in-plane coherence length d increase with increasing film thickness h.[22,25,28] $w(h)$ continues to increase until the growth front abruptly breaks down in an irreversible transition to amorphous layer growth.[30–32] Critical epitaxial thicknesses $h_1(T_s)$ for the onset of this transition, defined here as the film thickness at which bulk structural defects are first observed by reflection high-energy electron diffraction (RHEED) and cross-sectional transmission electron microscopy (XTEM), increase exponentially with film growth temperature T_s. As $h \rightarrow h_1$, deep cusps form at the base of interisland trenches and epitaxial breakdown is initiated as the surface roughness reaches a critical, T_s-independent, aspect ratio.[14,16,28]

In this article, we present results on the microstructural and surface morphological evolution of fully strained metastable heteroepitaxial $Ge_{1-x}Sn_x/Ge(001)$ layers as a function of x. Film growth temperatures in these experiments were maintained at $T_s = 155$ °C due to the combination of limited epitaxial thickness at lower temperatures and Sn surface segregation at higher temperatures.[15,16] High-resolution x-ray diffraction (HR-XRD) and reciprocal-space lattice mapping (RLM) measurements combined with XTEM show that for $h \leqslant h_1$, all films appear structurally perfect and fully commensurate with the substrate, while *in situ* angle-resolved x-ray photoelectron spectroscopy (AR-XPS) measurements reveal no measurable Sn segregation. Surface structural transitions during growth were monitored using *in situ* RHEED together with postdeposition atomic force microscopy (AFM) and XTEM.

Our results demonstrate that the incorporation of Sn in Ge mediates surface morphological evolution during film growth through two competing effects. At very low concentrations ($x \lesssim 0.020$), the dominant result is a Sn-induced enhancement in both the Ge adatom mobility and the rate of interlayer mass transport, thereby suppressing kinetic roughening and resulting in significant increases in the critical thickness h_1 for the onset of epitaxial breakdown. With $C_{Sn} = 4.4 \times 10^{20}$ cm^{-3} ($x = 0.010$), for example, the surface width w normalized to h_1 decreases from 2.6×10^{-3} for pure Ge(001) to 1.5×10^{-3}, while h_1 increases from $\simeq 7700$ Å to 1.40 μm. Moreover, layers for which $h_1 \rightarrow \infty$ are obtained with Sn concentrations between $\simeq 1 \times 10^{18}$ and 4.4×10^{20} cm^{-3}. However for $C_{Sn} > 8.8 \times 10^{20}$ cm^{-3} ($x > 0.020$), strain-induced roughening overcomes the Sn-induced surface smoothening effects and gives rise to a rapid decrease in h_1, which ranges from $\simeq 5700$ Å with $x = 0.029$ to 2350 Å with $x = 0.061$.

II. EXPERIMENTAL PROCEDURE

All $Ge_{1-x}Sn_x/Ge(001)$ layers were grown in a load-locked multichamber MBE system with a base pressure of 5×10^{-11} Torr. Ge (99.9999% pure) and Sn (99.999%) were evaporated from separate BN effusion cells whose temperatures were maintained constant to within ±1 °C using proportional-band feedback control. The combination of a quartz-crystal microbalance and an electron-impact emission sensor, calibrated based upon film thicknesses measured by microstylus profilometry, provides continuous *in situ* measurements of film growth rates R. Surface structural transitions were monitored *in situ* by RHEED utilizing a 20 kV primary electron beam that intersects the sample at an incidence angle of $\simeq 2°$. Images are acquired using an oscilloscope camera.

The substrates are polished 1.5×2.5 cm^2 Ge(001) plates cleaved from 0.5-mm-thick n-type wafers with a miscut of 0.1° in the [110] direction and room-temperature resistivities of 1–20 Ω cm ($n = 1 \times 10^{15}$–6×10^{13} cm^{-3}). Substrate cleaning consists of rinsing in deionized water to remove the native oxide followed by repeated cycles of oxidation, via a UV-ozone process,[33] and oxide dissolution, with the final step being the formation of a clean protective UV-ozone oxide cap layer. The wafers are then bonded to a Mo platen with In and immediately inserted into the UHV system where they are degassed at 250 °C for 45 min, following which the oxide is desorbed at $T_s \geqslant 450$ °C. This procedure provides clean Ge surfaces with sharp 2×1 RHEED patterns and no impurities detectable by *in situ* Auger or x-ray photoelectron spectroscopy measurements. Prior to $Ge_{1-x}Sn_x(001)$ film growth, 600-Å-thick Ge buffer layers are deposited at a rate R_{Ge} of 0.5 Å s^{-1} with $T_s = 400$ °C. The resulting Ge(001) surfaces also exhibit 2×1 RHEED patterns with sharp Kikuchi lines, indicating atomically smooth surfaces. Average terrace lengths are $\gtrsim 800$ Å as measured by scanning tunneling microscopy (STM).[22,25]

Homoepitaxial Ge(001) and heteroepitaxial $Ge_{1-x}Sn_x/Ge(001)$ overlayers were grown at $T_s = 155$ °C with R_{Ge} maintained constant at 0.5 Å s^{-1}, while the Sn deposition rate was set to obtain the desired x values ($\lesssim 0.06$). Film growth temperatures, controlled via the substrate heater power, were calibrated using thermocouples bonded to dummy substrates. The system was recalibrated periodically to correct for thermal drift. Sample temperatures during growth were maintained constant to within ±5 °C and absolute values are accurate to within ±10 °C.

The microstructure and crystalline quality of the layers were investigated using HR-XRD, high-resolution RLM (HR-RLM), XTEM, and high-resolution XTEM (HR-XTEM). The HR-XRD measurements were performed using a Philips X-Pert diffractometer with line-focused Cu $K_{\alpha 1}$ radiation ($\lambda = 1.540\,597$ Å) from a four-crystal Ge(220) monochromator, which provides an angular divergence of <12 arc s with a wavelength spread $\Delta\lambda/\lambda \simeq 7 \times 10^{-5}$. A laterally graded parabolic x-ray mirror between the source and the monochromator further enhanced beam collimation. ω-2θ overview scans were obtained with a detector acceptance angle of $\simeq 2°$, while an additional two-crystal Ge(220) ana-

lyzer was placed between the sample and the detector to obtain high-resolution (detector acceptance angle $\simeq$12 arc s) scans and reciprocal lattice maps about both symmetric and asymmetric reflections. The maps are generated by taking repetitive ω-2θ rocking curve scans starting at different initial values for ω.

XTEM and HR-XTEM examinations were carried out in Philips CM12 and Hitachi H-9000 microscopes operated at 120 and 300 kV, respectively. Specimens were prepared by gluing two samples film-to-film and then cutting a vertical section which was thinned to $\simeq$20 μm by mechanical grinding. Final thinning to electron transparency was accomplished by Ar^+ ion milling in a liquid-N_2-cooled stage with the incident beam angle and energy progressively reduced from 10° to 8° and 5 to 1.5 kV in order to obtain samples with relatively uniform thickness distributions.

Sn concentrations in doped Ge(001) layers ($C_{Sn} \leqslant 6 \times 10^{19}$ cm^{-3}) were determined using a Cameca IMS-5F secondary-ion mass spectrometer (SIMS) operated with a 12.5 keV Cs^+ primary ion beam. Quantification, with an experimental uncertainty of ±10%, was accomplished by comparison to Sn-ion-implanted bulk Ge(001) standards. $Ge_{1-x}Sn_x$(001) alloy layer thicknesses and compositions were measured by HR-XRD (for films with $x \gtrsim 0.001$) and Rutherford backscattering spectrometry (RBS) ($x \gtrsim 0.01$). The relative positions of substrate and film peaks obtained from HR-XRD ω-2θ scans and reciprocal lattice maps were used to calculate film compositions assuming Vegard's rule. Film thicknesses were determined from the angular spacing between finite-thickness interference fringes in ω-2θ scans. The RBS probe beam consisted of 2-MeV He^+ ions incident at an angle of 15° relative to the sample surface normal with the detector set at a 150° scattering angle. Backscattered spectra were analyzed using the RUMP simulation program.[34] Film compositions deduced from HR-XRD and RBS analyses were in excellent agreement with reported values being accurate to within ±0.3%.

AR-XPS measurements of as-deposited $Ge_{1-x}Sn_x$(001) layers were carried out *in situ* using a dual-anode source Perkin-Elmer PHI 5300 instrument with Mg K_α radiation ($h\nu$=1253.6 eV). Core-level spectra were obtained as a function of take-off angle φ, which was varied between 15° and 80° from the sample surface, using a pass energy of 17.9 eV with 0.05 eV steps. These conditions result in a spectral resolution of $\simeq$0.7 eV. After background subtraction following the procedure due to Shirley,[35] the peaks were fit using the CASA-XPS nonlinear least-squares software.[36]

AFM, operated in tapping mode, was used to follow the surface morphological evolution of as-deposited Ge(001) and $Ge_{1-x}Sn_x$(001) layers. The measurements were carried out in air using oxide-sharpened Si tips having average radii of 50–100 Å. Images were linearly planarized to remove sample tilting effects. The surface roughness was quantified using the height-height $H(\rho)=\langle h_i h_j \rangle$ and height-difference correlation functions $G(\rho)=\langle |h_i - h_j|^2 \rangle$, where h is the height at positions i and j separated by a distance ρ and the brackets correspond to averages over the measured surface. The mean interisland separation d is extracted from the position of the first local maximum in $H(\rho)$. The correlation functions are related to the surface width w, which is equivalent to the rms roughness, through the relationship $2w^2 = G(\rho) + 2H(\rho)$. $[G(\rho \to \infty)]^{1/2}$ is directly proportional to w in these experiments since $H(\rho \to \infty) \to 0$, consistent with STM results showing that the high-temperature Ge buffer layers are extremely flat.[22,25] Values of w and d were obtained by averaging over at least three different 1×1 μm^2 regions of each sample. At all film compositions except those for which $h_1 \to \infty$, the average roughening rate w/h is determined at $h = h_1$. Over the composition range in which $h_1 \to \infty$, w/h is determined using w and h values measured for layers with the highest film thickness. Two-dimensional (2D) slope histograms were constructed from the vector normals to the surface at all points in the AFM images and are plotted with increasing surface angle from the center of the image.

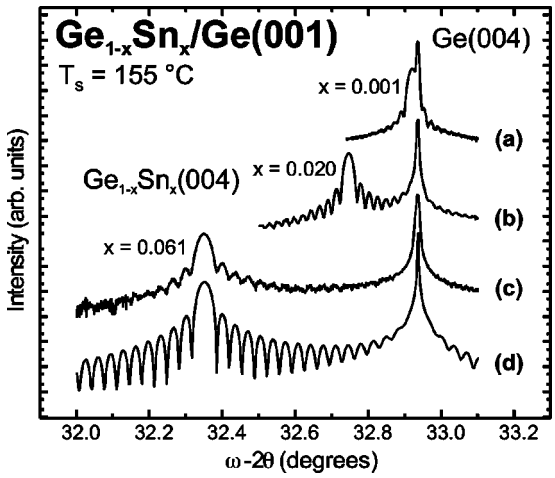

FIG. 1. HR-XRD ω-2θ scans about the Ge(004) Bragg reflection of $Ge_{1-x}Sn_x$/Ge(001) alloys with thicknesses h and Sn concentrations x of: (a) h=3000 Å and x=0.001, (b) h=2300 Å and x=0.020, and (c) h=1650 Å and x=0.061. (d) Fully dynamical simulation of the HR-XRD ω-2θ scan shown in (c). The curves have been shifted vertically for clarity.

III. EXPERIMENTAL RESULTS

$Ge_{1-x}Sn_x$ layers were grown on Ge(001) substrates at T_s=155 °C as a function of Sn concentration ($0 \leqslant x \leqslant 0.061$) and layer thickness (1650 Å $\leqslant h \leqslant$ 1.91 μm). Typical HR-XRD ω-2θ scans through substrate and film 004 Bragg peaks are presented in Fig. 1 for $Ge_{1-x}Sn_x$(001) alloys with x=0.001, 0.020, and 0.061. Fig. 1(a) is from a 3000-Å-thick, x=0.001 ($C_{Sn}=6\times10^{19}$ cm^{-3}) layer. The negative angular separation between substrate and layer peaks demonstrates that the film is in a state of in-plane compression. The layer peak position corresponds to an out-of-plane lattice parameter $a_\perp$=5.6599 Å (compared to a_o=5.6576 Å for pure Ge) and a misfit strain $\varepsilon = 1.4\times10^{-4}$. Increasing the Sn concentration raises the degree of in-plane compression as shown by the continuous increase in the angular separation between substrate and layer peaks in Figs. 1(a)–1(c). As x is raised to 2.0 and 6.1 at. %, $a_\perp$ increases to 5.6868 Å (ε =0.0029) and 5.7569 Å (ε=0.0090), respectively.

Finite-thickness fringes, which arise due to interference of diffracted waves scattered from a finite number of lattice planes, are observed in the regions surrounding the substrate and layer diffraction peaks in Figs. 1(a)–1(c). The fringes are

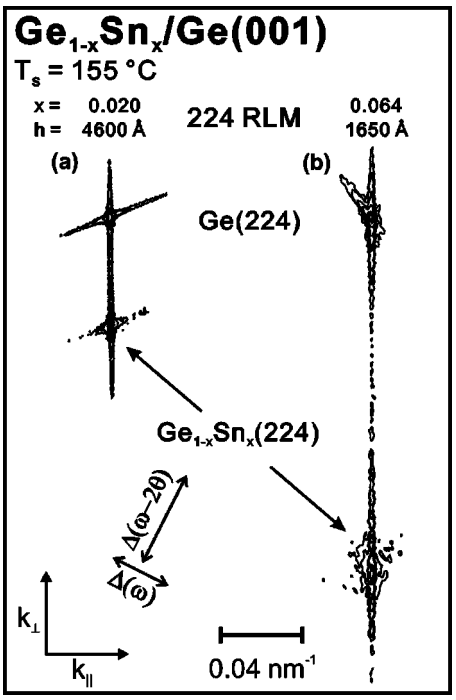

FIG. 2. HR-XRD reciprocal lattice maps around the 224 Bragg peak of $Ge_{1-x}Sn_x/Ge(001)$ alloys grown at $T_s=155$ °C with layer thicknesses h and Sn concentrations x of (a) $h=4600$ Å and $x=0.020$ and (b) $h=1650$ Å and $x=0.064$.

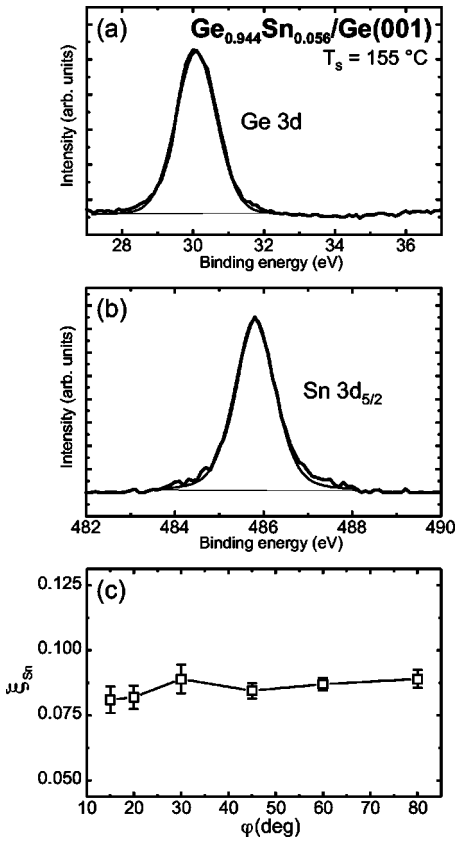

FIG. 3. (a) Ge $3d$ and (b) Sn $3d_{5/2}$ photoelectron spectra obtained *in situ* from a 1860-Å-thick $Ge_{0.944}Sn_{0.056}(001)$ layer grown at $T_s=155$ °C. (c) Normalized Sn intensity peak ratio $\xi_{Sn}=I_{Sn}/(I_{Sn}+I_{Ge})$ vs take-off angle φ.

a measure of the very high structural quality of the doped and alloyed layers, while indicating that lattice planes and interfaces are uniform and flat.[37] From the fringe spacings, we obtain layer thicknesses that are in very good agreement with growth rate calibrations. Simulated HR-XRD scans, based upon the fully dynamic formalism of Tagaki[38] and Taupin,[39] exhibit excellent agreement with experimental results for all samples, including those shown in Fig. 1. The simulations were carried out assuming perfectly abrupt and coherent film/buffer layer interfaces and linearly interpolated elastic constants. An example is presented in Fig. 1(d) corresponding to the sample in Fig. 1(c). The positions and intensities of the Bragg peaks as well as the finite-thickness fringes in the measured and simulated patterns agree extremely well. From the simulated results, we obtain, assuming Vegard's rule, Sn concentrations of 0.14, 1.99, and 6.15 at. % for the layers corresponding to Figs. 1(a)–1(c), respectively. This is consistent with SIMS and RBS values of 0.12 (6×10^{19} cm^{-3}), 1.9, and 6.2 at. %, respectively.

All $Ge_{1-x}Sn_x(001)$ alloy layers with $h\leqslant h_1$ are completely coherent with their substrates, as determined by HR-RLM and XTEM analyses. Figures 2(a) and 2(b) show typical HR-RLMs around asymmetric 224 reflections from $Ge_{0.980}Sn_{0.020}$ and $Ge_{0.936}Sn_{0.064}$ films grown to $h=4600$ and 1650 Å, respectively. Diffracted intensity distributions are plotted as isointensity contours as a function of the reciprocal lattice vectors $k_{\|}$ parallel and $k_{\perp}$ perpendicular to the surface. The transverse diffraction intensity distributions across the substrate and layer peaks in Fig. 2(a) and the substrate peak in Fig. 2(b) are due to residual scattering from the analyzer crystal and monochromator, respectively.[40,41] The substrate and film peaks from all samples in this study, irrespective of x, are perfectly aligned along the $k_{\|}$ direction with an in-plane strain relaxation below the instrument detection limit of $\simeq1\times10^{-5}$. The diffraction contours in Fig. 2 are nearly symmetric, with the exception of the elongation in the substrate peak along the growth direction due to the presence of the interface, which breaks the crystal periodicity.

The layers in Figs. 2(a) and 2(b) are under compressive strain with out-of-plane lattice constants of $a_{\perp}=5.6855$ Å and $a_{\perp}=5.7502$ Å for $x=0.020$ and 0.064, respectively, which concurs with the HR-XRD results (5.6868 Å and 5.7569 Å). Finite-thickness interference fringes are clearly visible as periodic intensity contours along $k_{\perp}$. Assuming Vegard's rule and linearly interpolated elastic constants, the position of the alloy 224 peak corresponds to Sn fractions in the films of 0.0192 and 0.0645, in excellent agreement with values obtained from HR-XRD and RBS analyses.

In situ AR-XPS analyses demonstrate that there is no measurable Sn surface segregation in $Ge_{1-x}Sn_x(001)$ layers with thicknesses $h\leqslant h_1(x)$. The take-off angle φ, referenced to the sample surface, was varied between 15° and 80° corresponding to probe depths ranging from 16 to 59 Å, assuming an average photoelectron inelastic mean free path λ of 20 Å (Ref. 38) and an escape length of 3λ.

Figure 3(a) is a typical Ge $3d$ photoelectron spectrum, acquired at $\varphi=15°$, from a 1860-Å-thick $Ge_{0.944}Sn_{0.056}(001)$ layer. The spectrum, fit with a single curve, is a convolution of the Ge $3d_{5/2}$ and Ge $3d_{3/2}$ peaks arising from Ge atoms bonded only to other Ge atoms and the corresponding peaks

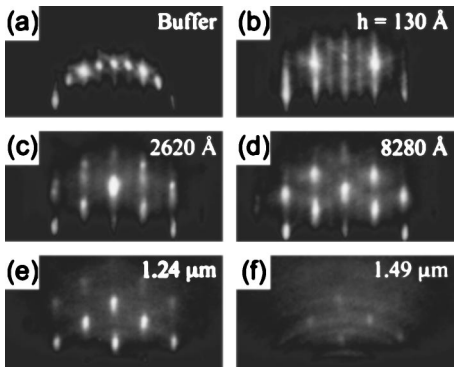

FIG. 4. RHEED patterns obtained along the [110] azimuth: (a) following MBE growth of a 600-Å-thick Ge buffer layer on Ge(001) at 400 °C and during growth of $Ge_{0.983}Sn_{0.017}$(001) at T_s=155 °C with R_{Ge}=0.5 Å s^{-1} to thicknesses (b) h=130, (c) 2620, (d) 8280, (e) 12 400, and (f) 14 900 Å.

from Ge bonded to Sn atoms since the peak separations ($\lesssim$0.3 eV)[42] are below the instrument resolution. The full width at half-maximum intensity Γ_{Ge} and the Gaussian-Lorentzian factor $G/(G+L)$ for the Ge peak are Γ_{Ge} =1.34 eV and $G/(G+L)$=85%, respectively. The peak maximum occurs at 30.12±0.07 eV. A corresponding Sn $3d_{5/2}$ spectrum from the same sample is shown in Fig. 3(b). The data are well fit using a single peak centered near 485.8 eV. We obtain a binding energy of 485.82 eV for Sn $3d_{5/2}$ with Γ_{Sn}=1.07 eV and $G/(G+L)$=65%.

The relative integrated intensities of the Ge and Sn XPS signals as a function of φ, accounting for the Ge $3d$ and Sn $3d_{5/2}$ sensitivity factors, are 0.226 and 3.496, respectively.[43] The Ge $3d$ and Sn $3d_{5/2}$ peak areas are then normalized and the ratio of their intensities, $\xi_{Sn}=I_{Sn}/(I_{Sn}+I_{Ge})$, is plotted as a function of φ for $Ge_{0.944}Sn_{0.056}$(001) as shown in Fig. 3(c). ξ_{Sn} remains essentially constant to within experimental uncertainty, independent of the take-off angle, at a value of $\simeq$0.085±0.004. This indicates the absence of measurable Sn surface segregation.

We use a combination of RHEED, XTEM, and AFM to follow the surface morphological evolution of $Ge_{1-x}Sn_x$(001) alloys and to measure h_1, the film thickness corresponding to the onset of epitaxial breakdown, as a function of x. RHEED observations show that surface roughness increases with film thickness at rates that depend on the Sn concentration. Typical RHEED results, obtained along the [110] azimuth, as a function of film thickness h are shown in Fig. 4 for $Ge_{0.983}Sn_{0.017}$(001) layers. Patterns from buffer layers [e.g., Fig. 4(a)] consist of sharp 2×1 spots, with nearly equi-intense fundamental and half-order features, characteristic of a very flat surface. During LT-MBE growth, the diffraction features become streaky, the half-order intensities gradually decrease, diffuse scattering increases, and the fundamental diffraction rods broaden. An example is shown in Fig. 4(b), corresponding to a $Ge_{0.983}Sn_{0.017}$(001) layer with h=130 Å. The observed changes as a function of h are indicative of a continuous decrease in the average size of 2×1 reconstructed terraces, increasing step densities, and atomic-scale surface roughening.[44,45] With further deposition, vertical intensity modulations become visible along the length of the fundamental diffraction rods, the signature of island formation in a multilayer 2D growth mode[46] [see, for example, Fig. 4(c) corresponding to h=2620 Å]. The modulations continue to increase in intensity with increasing layer thickness. $\frac{1}{3}$-order satellite reflections appear at $h=h_1$=8280 Å [Fig. 4(d)], signifying the formation, as confirmed by HR-XTEM (see later discussion), of 111 stacking faults and microtwins. $h_1(x)$ is determined from RHEED images as the film thickness at which twin reflections are first observed.

As the surface continues to roughen during deposition with $h>h_1$, the half-order streaks disappear, diffuse scattering increases, and the RHEED pattern gradually transforms to being three-dimensional, as shown in Fig. 4(e), corresponding to h=1.24 μm. The bulk diffraction spots are broad and elongated along the [001] growth direction. The broadening is inversely related to the mean interisland separation, while the elongation along [001] indicates that the average island height is less than the lateral size. Continued deposition gives rise to a decrease in the aspect ratio of the bulk diffraction spots as the islands grow faster in the vertical than the lateral direction. The diffracted beams are also increasingly triangular shaped. With further deposition, the bulk RHEED diffraction spots gradually decrease in intensity, signaling the formation of the amorphous phase [see, for example, Fig. 1(f) corresponding to h=1.49 μm].

The surface roughening process follows a similar pathway in films with higher Sn concentrations, but occurs more rapidly. However, compared to pure Ge(001), the addition of Sn in concentrations <2.0 at. % leads to a reduction in the overall roughening rate. Furthermore, RHEED patterns from $Ge_{1-x}Sn_x$(001) layers with Sn concentrations of 1×10^{18} -4.4×10^{20} cm^{-3} ($x=2.3\times10^{-5}-0.010$) show no indication of twinning or transforming to the amorphous phase for samples up to the highest thickness measured (1.9 μm); i.e., $h_1\rightarrow\infty$ for these samples.

HR-XTEM images from all samples reveal that 111 lattice fringes are continuous through the coherent film/substrate interface. Typical bright-field [110] zone-axis XTEM and HR-XTEM micrographs illustrating the sequence of structural changes observed as a function of layer thickness and Sn concentration, are shown in Fig. 5. The addition of Sn concentrations <1.0 at. % results in infinitely thick epitaxial layers ($h_1\rightarrow\infty$), in agreement with RHEED results, with no indication of extended defects, as demonstrated, for example, in Fig. 5(a) with h=1.8 μm and x=0.001. The selected area electron diffraction (SAED) pattern in the inset was obtained near the [110] zone axis and consists of single-crystal reflections with symmetric intensities.

In contrast to $Ge_{1-x}Sn_x$(001) layers with Sn concentrations x between 1×10^{18} and 4.4×10^{20} cm^{-3}, deposition of both pure Ge(001) and $Ge_{1-x}Sn_x$(001) layers with $x\geqslant0.010$ results in the formation of three distinct regions leading eventually to epitaxial breakdown. The first region is a defect-free sublayer, as judged by both XTEM and HR-XTEM, extending to h_1, which we define as the layer thickness at which bulk structural defects are first observed. h_1 values were obtained from examination of several micrographs, corresponding to >2 μm of interface, for each sample investigated. An example is shown in Fig. 5(b) for a 6300-Å-thick $Ge_{0.945}Sn_{0.055}$(001) sample with h_1=2350 Å.

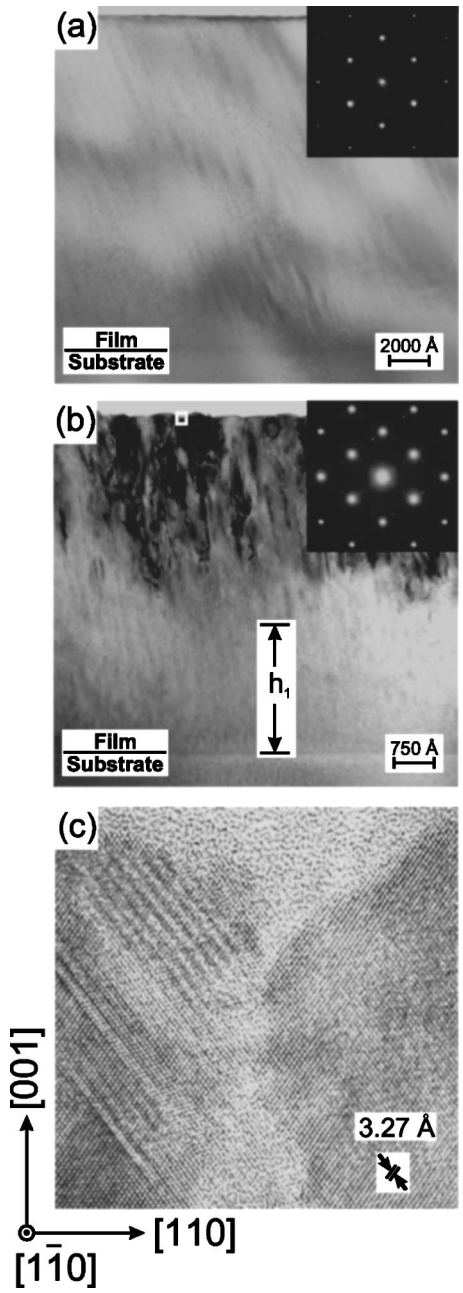

FIG. 5. [110] bright-field zone-axis XTEM micrographs of $Ge_{1-x}Sn_x$ layers grown on Ge(001) by LT-MBE at $T_s=155$ °C with $R_{Ge}=0.5$ Å s^{-1} to thicknesses h. (a) $Ge_{0.999}Sn_{0.001}$, $h=1.8$ μm and (b) $Ge_{0.945}Sn_{0.055}$, $h=6300$ Å. (c) is a HR-XTEM image of the region outlined by the small open white square in (b).

Continuing deposition to $h>h_1$ leads to the formation of a defective, but still epitaxial, region containing 111 stacking faults, which are initiated by double-positioning defects on {111} facet planes and microtwins.[28] This is shown by the inset of Fig. 5(b), which consists of a [110] zone-axis SAED pattern with characteristic $\frac{1}{3}$-order satellite reflections arising from twinning along 111 directions. Further evidence of twinning is shown in Fig. 5(c), which is a HR-XTEM image of the region outlined by the small white square near the surface of the film in Fig. 5(b). With further deposition, the growth mode transforms to an amorphous overlayer with a columnar microstructure (not shown). The interface between the defective epitaxial region and amorphous phase is, although locally atomically abrupt, globally rough and triangular shaped (in a 2D projection), with {111} facets.

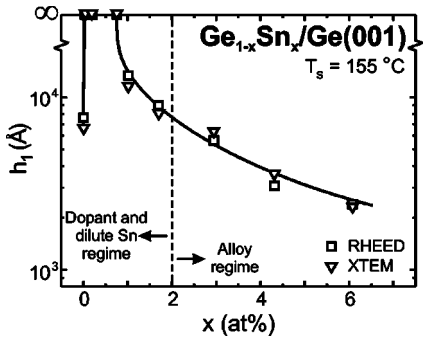

FIG. 6. Critical epitaxial thickness h_1 as a function of the Sn fraction x in $Ge_{1-x}Sn_x$ layers grown on Ge(001) at $T_s=155$ °C. The range in x over which $h_1\rightarrow\infty$ is $1\times10^{18}\leqslant x<4.4\times10^{20}$ cm^{-3}.

Figure 6 is a plot of h_1 versus x for $Ge_{1-x}Sn_x(001)$ LT-MBE layers grown at $T_s=155$ °C. Results obtained from RHEED and XTEM are in excellent agreement over the entire Sn concentration range. The critical epitaxial thickness h_1, which is $\simeq$7700 Å for pure Ge, becomes infinite with the addition of Sn in dopant quantities ($1\times10^{18}\leqslant x<4.4\times10^{20}$ cm^{-3}). As the Sn concentration is increased further, h_1 again becomes finite and decreases from 1.40 μm with $x=0.010$, to 5700 Å with $x=0.029$, and 2350 Å with $x=0.061$. Thus, the $h_1(x)$ data for $Ge_{1-x}Sn_x(001)$ layers indicates the presence of at least two competing effects. With $x\leqslant0.02$ (dopant/dilute-Sn regime), the addition of Sn results in an increase in h_1 compared to that for pure Ge(001) LT-MBE, while Sn concentrations greater than 0.02 (alloying regime) lead to a reduction in the epitaxial thickness.

AFM results were used to provide a quantitative measure of $Ge_{1-x}Sn_x(001)$ surface morphological evolution as a function of x. Figures 7(a)–7(f) are typical AFM images and corresponding 2D slope histograms obtained from $Ge_{1-x}Sn_x(001)$ layers grown at $T_s=155$ °C with Sn concentrations ranging from 0 to 6.1 at. %. Black-to-white gray scale values Δz were chosen to be four times the standard deviation of the height distribution around the average value, and are therefore proportional to the surface width w. Ge(001) and $Ge_{1-x}Sn_x(001)$ layers with $x\gtrsim0.010$ (4.4×10^{20} cm^{-3}) were grown to thicknesses $h\simeq h_1(x)$ as shown in Figs. 7(a) and 7(d)–7(f), while Figs. 7(b) and 7(c) are AFM images of $Ge_{0.999}Sn_{0.001}$ and $Ge_{0.993}Sn_{0.007}(001)$ layers, for which $h_1\rightarrow\infty$, grown to thicknesses of 1.80 and 1.71 μm, respectively.

From Fig. 7, it is clear that the pathway for $Ge_{1-x}Sn_x(001)$ surface roughening is strongly dependent on the Sn concentration. The surface morphology of layers with $x\leqslant0.020$ consists of regular arrangements of pyramidal islands with square bases [see Figs. 7(a)–7(d) with $h=7500$ Å to 1.8 μm] which tend to self-align along elastically soft[47] ⟨100⟩ directions. As x is continuously increased from 0 to 1.0 at. %, the pyramidal structures decrease in size, become more well-defined, and exhibit enhanced self-organization. Compare, for example, Fig. 7(a) corresponding to pure Ge ($h=7500$ Å) with Fig. 7(c), for which $x=0.007$ ($h=1.71$ μm). Thus, the surface roughness and mean inter-

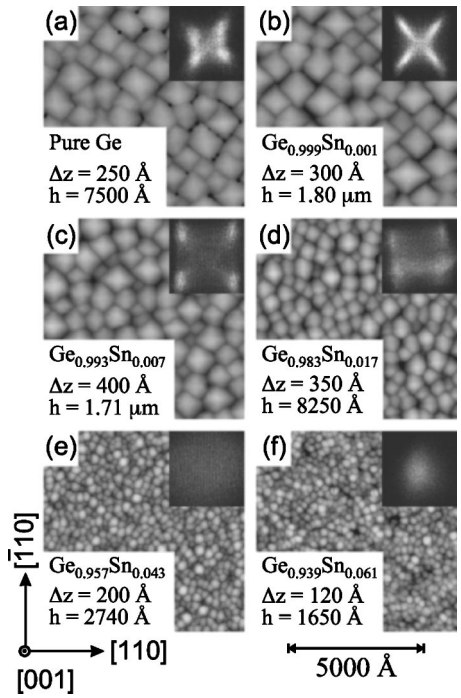

FIG. 7. AFM images of the surface of $Ge_{1-x}Sn_x/Ge(001)$ layers grown by LT-MBE at $T_s=155$ °C with $R_{Ge}=0.5$ Å s^{-1}. Film compositions x, thicknesses h, and black-to-white gray Δz scales are: (a) $x=0$, $h=7500$ Å, and $\Delta z=250$ Å, (b) $x=0.001$, $h=1.80$ μm, and $\Delta z=300$ Å, (c) $x=0.007$, $h=1.71$ μm, and $\Delta z=400$ Å, (d) $x=0.017$, $h=8250$ Å, and $\Delta z=350$ Å, (e) $x=0.043$, $h=2740$ Å, and $\Delta z=200$ Å, and (f) $x=0.061$, $h=1650$ Å, and $\Delta z=120$ Å. Insets are 2D slope histograms, ranging over ±25° in the x and y directions, showing the directions of surface vector normals.

island separation decrease in the presence of dilute Sn concentrations. At $x>0.020$, the surface features are transformed from pyramidal islands to round mounds [Figs. 7(d) and 7(e)]. Deposition to $h\simeq h_1$ at still higher Sn concentrations leads to smaller, more compact, and better-defined mounds as shown in Fig. 7(f) corresponding to $x=0.061$ with $h=1650$ Å. Despite the smaller mound size, the average roughening rate w/h_1 increases with $x>0.020$ due to strain-induced effects as discussed subsequently.

Slope histograms for pure Ge(001) layers with $h=7500$ Å [see inset in Fig. 7(a)] are characterized by intensity distributions that are primarily contained within lobes which range out along the four ⟨100⟩ in-plane directions at angles up to 7.5°. This indicates a tendency for faceting, consistent with the corresponding AFM images revealing pyramid-shaped structures. As the Sn concentration is increased to 0.001 (6.1×10^{19} cm^{-3}) and subsequently to 0.007 (3.1×10^{20} cm^{-3}), there is a marked decrease in intensity near the [001] pole and most of the intensity in the slope histograms in Figs. 7(b) ($x=0.001, h=1.8$ μm) and 7(c) ($x=0.007, h=1.71$ μm) is contained within lobes extending out to ≃9.2° and 11.5°, respectively, along ⟨100⟩ and ⟨010⟩ directions. This demonstrates that the propensity toward faceting is greatly enhanced with increasing x, and the amount of flat surface area between trenches decreases significantly. The increase in island sidewall angle with increasing Sn concentration suggests a tendency toward the development of {105} facets (polar angle $\phi=11.3°$). Further increases in x to 0.017 ($h=8250$ Å) results in the 2D slope histogram becoming increasingly diffuse [inset in Fig. 7(d)], indicating a wider distribution of surface slopes. As x exceeds 0.020, the slope histograms evolve towards a Gaussian intensity distribution [see, for example, the insets in Fig. 7(e) and 7(f)] as the pyramid-shaped structures transform to rounded growth mounds. $Ge_{0.939}Sn_{0.061}(001)$ slope histograms [Fig. 7(f), $h=1650$ Å] are characterized by intensity distributions centered within ≲5.3° of the center pole, indicating that local surface slopes are relatively shallow.

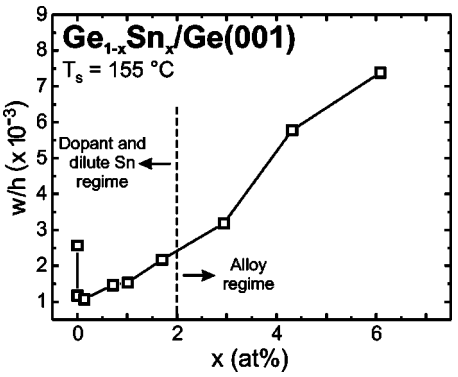

FIG. 8. Average roughening rate w/h vs the composition x of epitaxial $Ge_{1-x}Sn_x$ layers grown on Ge(001) at $T_s=155$ °C.

The surface width w at h_1 initially increases with the addition of Sn in dopant quantities, ranging from 20.1 Å for pure Ge(001) to 25.1 Å for $Ge_{0.993}Sn_{0.007}(001)$ due to a corresponding increase in $h_1(x)$ that allows for additional island coalescence. However, as demonstrated in Fig. 8, there is an initial, marked decrease in the average roughening rate w/h with increasing Sn doping. w/h decreases from 2.6×10^{-3} for pure Ge to 1.5×10^{-3} with $x=0.010$ ($C_{Sn}=6\times10^{19}$ cm^{-3}). As the Sn concentration is further increased above $x=0.010$, there is a continuous decrease in the surface width at h_1. $w(h_1)$ decreases from 21.4 Å for a 1.40-μm-thick $Ge_{0.990}Sn_{0.010}$ layer to 15.4 Å for a 2080-Å-thick $Ge_{0.939}Sn_{0.061}(001)$ alloy. While $w(h_1)$ decreases with increasing x over the Sn concentration range $0.010\leqslant x\leqslant0.061$ due to a continuous reduction in h_1, the normalized value w/h rapidly increases from 1.5×10^{-3} with $x=0.010$, to 7.4×10^{-3} with $x=0.061$. Figure 8 shows that, compared to pure Ge(001), Sn concentrations ≲2.0 at. % lead to a reduction in w/h while $C_{Sn}>2.0$ at. % results in an increase in w/h. The observed decrease (increase) in the average roughening rate corresponds with the enhancement (reduction) of $h_1(x)$, as indicated in Fig. 6. The mean interisland separation d at h_1 decreases continuously with increasing x over the entire Sn concentration range. $d(h_1)$ decreases from 1155 to 405 Å as x is increased from 0 to 6.1 at. %.

IV. DISCUSSION

We have grown epitaxial metastable $Ge_{1-x}Sn_x(001)$ layers with Sn concentrations ranging from 0 to 6.1 at. % at $T_s=155$ °C by solid-source MBE. All films with thicknesses $h\leqslant h_1(x)$, where h_1 is the film thickness corresponding to the onset of epitaxial breakdown, are structurally perfect, exhibit uniform Sn compositions with no indication of segregation, and are fully commensurate with their substrates, as deter-

mined by *in situ* RHEED and AR-XPS combined with post-deposition HR-XRD, HR-RLM, and XTEM measurements. For a given alloy concentration, the surface roughness increases continuously with film thickness h at a rate that depends on x. At Sn concentrations for which epitaxial breakdown occurs, continuing film growth to thicknesses $h > h_1(x)$ leads to the formation of a defective, but still epitaxial, sublayer containing 111 stacking faults and microtwins which, with increasing thickness, eventually transforms to an amorphous overlayer.

RHEED, AFM, and XTEM results show that the low growth temperature required to inhibit Sn segregation results in surface roughening that ultimately leads, for pure Ge and $Ge_{1-x}Sn_x(001)$ films with $x \gtrsim 0.01$, to epitaxial breakdown. $h_1(x)$ data for these layers can be categorized into one of two regimes indicating the presence of at least two competing effects. With $x \lesssim 0.02$ (dopant/dilute-Sn regime), the addition of Sn results in a decrease in the roughening rate w/h, and a corresponding increase in the critical epitaxial thickness, compared to pure Ge(001) LT-MBE. In fact, $h_1 \rightarrow \infty$ for layers with $2.3\times10^{-5} \leqslant x < 0.010$ $(1\times10^{18} \leqslant C_{Sn} < 4.4\times10^{20}\ cm^{-3})$. Sn concentrations greater than 0.02 (alloying regime) give rise to an increased rate of surface roughening and, hence, lower epitaxial thicknesses than that obtained for Ge(001). AFM micrographs reveal that surface morphology during $Ge_{1-x}Sn_x(001)$ LT-MBE evolves via the formation of a periodic array of growth mounds that tend to self-organize along $\langle 100\rangle$ directions. Alloys with $0 < x \lesssim 0.02$ form well-defined pyramidal islands bounded by {105} facets, while increasing x above 0.02 leads to a transformation in the mound shape from pyramidal structures to rounded mounds.

The two primary mechanisms that control surface morphological evolution during epitaxial growth are kinetic and strain-induced roughening. The former is associated with LT growth, while the latter typically takes place during higher temperature strained-layer heteroepitaxy. Kinetic roughening occurs when a significant fraction of adatoms condensing on the tops of islands cannot cross step edges to lower terraces before nucleating a new higher-level island. Thus, growth proceeds on multiple levels simultaneously. As deposition continues and the islands coalesce, trenches are formed between adjacent mounds. These trenches become deeper and wider (i.e., the amplitude of the roughness increases). As $h \rightarrow h_1$, deep cusps bounded by {111} facets form at the base of interisland trenches and epitaxial breakdown is initiated on these facets as the surface roughness reaches a critical T_s-independent aspect ratio.[28] Thus, continual filling of interisland trenches is the critical step for ensuring continuous epitaxial growth.

We have recently demonstrated that the incorporation of dilute quantities of Sn (e.g., $C_{Sn}=6\times10^{19}\ cm^{-3}$) during LT Ge(001) deposition increases $h_1(T_s)$ by up to an order of magnitude over the temperature range $T_s=95-125\ ^\circ C$.[14] The dramatic increase in $h_1(T_s)$ was attributed to enhancements in Ge step crossing probabilities and terrace migration mobilities. The resulting Sn-induced increase in interlayer mass transport gives rise to enhanced filling of interisland trenches which, in turn, decreases the rate of {111} facet formation. Bratland *et al.*[14] proposed that 2D segregation of Sn atoms (the Sn covalent radius $r_{Sn}=1.405$ Å, compared to $r_{Ge}=1.225$ Å for Ge) in surface islands leads to preferential attachment at step edges, thereby increasing the probability of itinerant Ge atoms crossing to lower terraces through a push-out/exchange mechanism similar to what has been observed by field-ion microscopy studies of adatom diffusion on metals.[48,49]

In the present experiments, carried out at $T_s=155\ ^\circ C$, we observe that the average sidewall angle of mounds formed on Ge(001) layers increases with increasing film thickness h until at $h=h_1\simeq7500$ Å, the surface morphology is defined by pyramid-shaped structures with sidewall angles of 7.5° as viewed along $\langle 100\rangle$ directions. This approximately corresponds to a {107} facet (polar angle $\phi=8.1°$) and is tending toward {105} facets ($\phi=11.3°$) that we observe for dilute $Ge_{1-x}Sn_x(001)$ alloys with $x \lesssim 0.02$. As discussed earlier the addition of Sn during Ge(001) LT-MBE enhances Ge interlayer mass transport which, in turn, leads to surface smoothening and enables sustained development of the surface morphology through increases in h_1. This is particularly evident in $Ge_{1-x}Sn_x(001)$ alloys with $1\times10^{18} \leqslant C_{Sn} < 4.4\times10^{20}\ cm^{-3}$ where $h_1 \rightarrow \infty$. For these samples, the surface never reaches a critical w/d value and, hence, epitaxial breakdown does not occur. Rather, fully formed {105}-faceted pyramids are obtained and, while w continues to increase with further growth, the surfaces remain self-similar. That is, the pyramidal islands continuously increase in size and coalesce, but exhibit no further change in sidewall angle. The stability of {105} facets, also observed to be the bounding planes of pyramidal islands formed on compressively strained $Si_{1-x}Ge_x/Si(001)$ surfaces,[50,51] has been attributed to repulsive step-step interactions.[52,53]

Increasing x in $Ge_{1-x}Sn_x/Ge(001)$ alloys corresponds to an increase in the total strain energy. Relaxation through strain-induced roughening becomes thermodynamically favorable when the energy cost associated with the increased surface area is overcome by the decrease in film strain energy due to dilatation in interplanar spacings near island peaks. Tersoff and LeGoues[54] showed that the activation energy for strain-induced roughening decreases rapidly with increasing misfit strain ε, varying as ε^{-4}. Thus, strain enhances the overall roughening rate by making it increasingly favorable for the film to elastically relax.

At small ε values, strain-induced roughening is highly constrained since the energy gain due to elastic relaxation is small compared with the energy cost associated with increased surface area. In the dopant regime ($C_{Sn} < 4.4\times10^{20}\ cm^{-3}$), where the surface morphology is controlled by kinetic roughening, the dominant effect is a Sn-induced smoothening of the surface and epitaxial breakdown no longer occurs. For $C_{Sn} \gtrsim 4.4\times10^{20}\ cm^{-3}$ ($x \gtrsim 1.0$ at. %), the strain due to Sn incorporation begins to play a role, although kinetic roughening still dominates. w/h increases with increasing x and h_1 again becomes finite. As C_{Sn} is increased from 1.0 to 2.0 at. % (i.e., ε is increased from 1.5×10^{-3} to 2.9×10^{-3}), there is a continuous reduction in h_1. However, w/h is still less than that for pure Ge(001) and, consequently, h_1 values for these alloys are higher than for Ge(001).

The low growth temperature used in these experiments

would normally be expected to kinetically inhibit strain-induced roughening, even in the presence of relatively large compressive strains, due to the necessity for massive uphill diffusion. However, as pointed out by Desjardins *et al.*,[16] kinetic roughening during the initial stages of LT heteroepitaxial growth provides gradients in the surface chemical potential which, although at small length scales, can be sufficient to initiate strain-induced roughening even at low temperatures. Thus, for Sn concentrations >2.0 at. %, strain-induced roughening overcomes the Sn-induced surface smoothening effects and results in an increase in the overall roughening rate and, hence, a reduction in h_1 compared to that of pure Ge(001). The onset of strain-induced roughening is manifested not only through an increase in the overall roughening rate, but also through a change in mound shape as the {105}-faceted pyramidal islands gradually become rounded mounds with increasing x. This shape transformation is initiated at $x \simeq 0.01$ and is complete for $x > 0.02$.

The fact that both the increase and the decrease we observe in $h_1(x)$ over different ranges in Sn concentrations are directly proportional to changes in the average roughening rate provides further evidence for the direct correlation between epitaxial breakdown and surface roughening, and indicates that breakdown itself is a growth mode transition that is driven by surface roughening.[14,28] Furthermore, the changes in Ge(001) growth kinetics due to Sn incorporation make it possible to controllably manipulate the surface roughening pathway, and hence the epitaxial thickness, over a very wide range by varying the Sn concentration through the dopant to dilute alloy concentration regime.

V. CONCLUSIONS

Microstructural and surface morphological evolution during LT-MBE growth ($T_s = 155$ °C) of $Ge_{1-x}Sn_x/Ge(001)$ layers were followed as a function of the Sn concentration x, which was varied from 0 through the doping and dilute alloy ranges up to 6.1 at. %. All layers with $h \leqslant h_1(x)$ are structurally perfect, exhibit no indication of Sn surface segregation, and are fully commensurate with their substrates. The addition of Sn during LT Ge(001) growth was found to mediate surface morphological evolution through two competing mechanisms. At very low Sn concentrations ($x \lesssim 0.02$), the dominant effect is a Sn-induced enhancement in both the Ge surface diffusivity and the probability of interlayer mass transport. This, in turn, results in more efficient filling of interisland trenches, and thus delays epitaxial breakdown. For $Ge_{1-x}Sn_x(001)$ layers with $1 \times 10^{18} \leqslant x < 4.4 \times 10^{20}$ cm^{-3}, the surface roughness never reaches the critical aspect ratio for the onset of breakdown and hence $h_1 \rightarrow \infty$. The surfaces of these samples consist of periodic arrays of faceted pyramidal islands that increase in size with further growth, but remain self-similar. At higher Sn concentrations, there is a change in growth kinetics due to a continuous increase in the amount of compressive strain. This leads, for $Ge_{1-x}Sn_x(001)$ layers with $x \gtrsim 4.4 \times 10^{20}$ cm^{-3} (1.0 at. %), to h_1 decreasing with increasing x. However, the overall roughening rate is still less than that for pure Ge(001) and, consequently, h_1 values are higher. This behavior is accompanied by a gradual transformation in the mound shape from faceted pyramids to rounded mounds. When the Sn concentration in $Ge_{1-x}Sn_x(001)$ exceeds 2.0 at. %, $h_1(x)$ falls below that of pure Ge(001) as strain-induced roughening overcomes the Sn-induced surface smoothening effects and results in an increase in the overall roughening rate. The thermal activation required for strain-induced roughening is partially overcome by the fact that kinetic roughening provides local surface chemical potential gradients which are sufficient to catalyze strain-induced roughening even at low growth temperatures.

Overall, we have shown that by varying the Sn concentration through the dopant to dilute alloy concentration range during LT Ge(001) growth, we can controllably manipulate the surface roughening pathway, and hence the epitaxial thickness, over a very wide range.

ACKNOWLEDGMENTS

The authors gratefully acknowledge the financial support of the U.S. Department of Energy (DOE) under Grant No. DEFG02-91ER45439 during the course of this research. They also appreciate the use of the facilities of the Center for Microanalysis of Materials, which is partially supported by the DOE, at the University of Illinois. One author (K. B.) thanks the Support for Under-Represented Groups in Engineering (SURGE) Fellowship Program at the University of Illinois. Another (P. D.) thanks the Canada Research Chair Program and the Natural Sciences and Engineering Research Council of Canada for financial support.

[1] M. Copel, M. C. Reuter, E. Kaxiras, and R. M. Tromp, Phys. Rev. Lett. **63**, 632 (1989).
[2] F. K. LeGoues, M. Copel, and R. M. Tromp, Phys. Rev. Lett. **63**, 1826 (1989).
[3] M. Copel, M. C. Reuter, M. Horn von Hoegen, and R. M. Tromp, Phys. Rev. B **42**, 011 682 (1990).
[4] D. J. Eaglesham, F. C. Unterwald, and D. C. Jacobson, Phys. Rev. Lett. **70**, 966 (1993).
[5] H. Nakahara and M. Ichikawa, Appl. Phys. Lett. **61**, 1531 (1992).
[6] M. Horn-von Hoegen, J. Falta, M. Copel, and R. M. Tromp, Appl. Phys. Lett. **66**, 487 (1995).
[7] B. Gallas, I. Berbezier, J. Chevrier, and J. Derrien, Phys. Rev. B **54**, 4919 (1996).
[8] B. Gallas, I. Berbezier, and J. Derrien, Thin Solid Films **294**, 69 (1997).
[9] B. Gallas, I. Berbezier, J. Derrien, D. Gandolfo, J. Ruiz, and V. A. Zagrebnov, J. Vac. Sci. Technol. B **16**, 1564 (1998).
[10] D. W. Jenkins and J. D. Dow, Phys. Rev. B **36**, 7994 (1987).
[11] K. A. Mäder, A. Baldereschi, and H. von Känel, Solid State Commun. **89**, 1123 (1989).
[12] G. He and H. A. Atwater, Phys. Rev. Lett. **79**, 1937 (1997).
[13] R. Ragan and H. A. Atwater, Appl. Phys. Lett. **77**, 3418 (2000).
[14] K. A. Bratland, Y. L. Foo, P. Desjardins, and J. E. Greene, Appl. Phys. Lett. **82**, 4247 (2003).
[15] O. Gürdal, P. Desjardins, J. R. A. Carlsson, N. Taylor, H. H. Radamson, J.-E. Sundgren, and J. E. Greene, J. Appl. Phys. **83**, 162 (1998).
[16] P. Desjardins, T. Spila, O. Gürdal, N. Taylor, and J. E. Greene, Phys. Rev. B **60**, 15993 (1999).
[17] P. R. Pukite, A. Harwit, andS. S. Iyer, Appl. Phys. Lett. **54**, 2142 (1989).
[18] W. Wegscheider, J. Olajos, U. Menczigar, W. Dondl, and G. Abstreiter, J. Cryst. Growth **123**, 75 (1992).
[19] J. Villain, J. Phys. I **1**, 19 (1991).
[20] J. Lapujoulade, Surf. Sci. Rep. **20**, 191 (1994).
[21] M. D. Johnson, C. Orme, A. W. Hunt, D. Graff, J. Sudijono, L. M. Sander, and B. G. Orr, Phys. Rev. Lett. **72**, 116 (1994).
[22] J. E. Van Nostrand, S. J. Chey, M.-A. Hasan, D. G. Cahill, and J. E. Greene, Phys. Rev. Lett. **74**, 1127 (1995).
[23] J. A. Stroscio, D. T. Pierce, M. D. Stiles, A. Zangwill, andL. M. Sander,

Phys. Rev. Lett. **75**, 1127 (1995).
[24]N.-E. Lee, D. Cahill, and J. E. Greene, Phys. Rev. B **53**, 7876 (1996).
[25]J. E. Van Nostrand, S. J. Chey, and D. G. Cahill, Phys. Rev. B **57**, 12536 (1998).
[26]B. W. Karr, I. Petrov, P. Desjardins, D. G. Cahill, and J. E. Greene, Surf. Coat. Technol. **94–95**, 12 536 (1998).
[27]C. Schelling, G. Springholz, and F. Schaffler, Thin Solid Films **369**, 1 (2000).
[28]K. A. Bratland, Y. L. Foo, J. A. N. T. Soares, T. Spila, P. Desjardins, and J. E. Greene, Phys. Rev. B **67**, 125322 (2003).
[29]G. Ehrlich and F. G. Hudda, J. Chem. Phys. **44**, 1039 (1966); S. C. Wang and G. Ehrlich, Phys. Rev. Lett. **70**, 41 (1993); **71**, 4177 (1993); G. Ehrlich, Surf. Sci. **331/333**, 865 (1995); A. Gölzhäuser and G. Ehrlich, Phys. Rev. Lett. **77**, 1334 (1996).
[30]N.-E. Lee, G. A. Tomasch, and J. E. Greene, Appl. Phys. Lett. **65**, 3236 (1994).
[31]N.-E. Lee, G. Xue, and J. E. Greene, J. Appl. Phys. **80**, 769 (1996).
[32]G. Xue, H. Z. Xiao, M.-A. Hasan, J. E. Greene, and H. K. Birnbaum, J. Appl. Phys. **74**, 2512 (1993).
[33]X.-J. Zhang, G. Xue, A. Agarwal, R. Tsu, M.-A. Hasan, J. E. Greene, and A. Rockett, J. Vac. Sci. Technol. A **11**, 2553 (1993).
[34]J. R. Doolittle, Nucl. Instrum. Methods Phys. Res. B **15**, 227 (1986).
[35]D. A. Shirley, Phys. Rev. B **5**, 4709 (1972).
[36]CasaXPS, Advanced Processing Software for XPS Spectra; Casa Software Ltd., Wilmslow, UK SK9 6SN.
[37]M. A. G. Halliwell, M. H. Lyons, S. T. Davey, M. Hockley, C. G. Tuppen, and C. J. Gibbings, Semicond. Sci. Technol. **4**, 10 (1989).
[38]S. Tagaki, Acta Crystallogr. **15**, 1311 (1962).
[39]D. Taupin, Bull. Soc. Fr. Mineral. Cristallogr. **87**, 469 (1964).
[40]P. Fewster, Semicond. Sci. Technol. **8**, 1915 (1993).
[41]H. Heinke, M. O. Moller, D. Hommel, and G. Landwehr, J. Cryst. Growth **135**, 41 (1994).
[42]*Handbook of X-ray Photoelectron Spectroscopy*, edited by J. Chastain and R. C. King, Jr. (Perkin-Elmer Corporation, Physical Electronics Division, Eden Prairie, MN, 1992).
[43]Inelastic mean free path values for Mg K_α excitation are 24.8 and 17.8 Å for Ge 3*d* and Sn $3d_{5/2}$, respectively; *NIST Electron Inelastic-Mean-Free-Path Database* Version 1.1; S. Tanuma, C. J. Powell, and D. R. Penn (unpublished data).
[44]M. G. Lagally, in *Methods of Experimental Physics*, edited by R. L. Park and M. G. Lagally (Academic, New York, 1985), Vol. 22.
[45]M. Henzler, in *Electron Spectroscopy for Surface Analysis*, edited by H. Ibach, in Topics in Current Physics, Vol. 4 (Springer, Berlin, 1977).
[46]C. Argile and G. E. Rhead, Surf. Sci. Rep. **10**, 227 (1989).
[47]V. A. Shchukin, N. N. Ledentsov, P. S. Kop'eV, and D. Bimberg, Phys. Rev. Lett. **75**, 2968 (1995).
[48]S. C. Wang and G. Ehrlich, Phys. Rev. Lett. **67**, 2509 (1991).
[49]Z. Zhang and M. G. Lagally, Phys. Rev. Lett. **72**, 693 (1994).
[50]N.-E. Lee, D. G. Cahill, and J. E. Greene, J. Appl. Phys. **80**, 2199 (1996).
[51]T. Spila, P. Desjardins, A. Vailionis, H. Kim, N. Taylor, D. G. Cahill, J. E. Greene, S. Guillon, and R. A. Masut, J. Appl. Phys. **91**, 3579 (2002).
[52]D. E. Jesson, K. M. Chen, and S. J. Pennycook, MRS Bull. **21**, 31 (1996).
[53]K. M. Chen, D. E. Jesson, S. J. Pennycook, T. Thundat, and R. J. Warmack, Phys. Rev. B **56**, R1700 (1997).
[54]J. Tersoff and F. K. LeGoues, Phys. Rev. Lett. **72**, 3570 (1994).